BBA - Proteins and Proteomics 1872 (2024) 140952

Contents lists available at ScienceDirect

BBA - Proteins and Proteomics

journal homepage: www.elsevier.com/locate/bbapap

Research Paper

Structural and functional characterisation of Tst2, a novel TRPV1 inhibitory peptide from the Australian sea anemone *Telmatactis stephensoni*

Khaled A. Elnahriry [a], Dorothy C.C. Wai [a], Lauren M. Ashwood [b,1], Muhammad Umair Naseem [c], Tibor G. Szanto [c], Shaodong Guo [d], Gyorgy Panyi [c], Peter J. Prentis [b,e], Raymond S. Norton [a,f,*]

[a] *Medicinal Chemistry, Monash Institute of Pharmaceutical Sciences, Monash University, Parkville, VIC 3052, Australia*
[b] *School of Biology and Environmental Science, Faculty of Science, Queensland University of Technology, Brisbane, QLD 4000, Australia*
[c] *Department of Biophysics and Cell Biology, Faculty of Medicine, University of Debrecen, Debrecen 4032, Hungary*
[d] *Institute for Molecular Bioscience, The University of Queensland, St Lucia, QLD 4072, Australia*
[e] *Centre for Agriculture and the Bioeconomy, Queensland University of Technology, Brisbane, QLD 4000, Australia*
[f] *ARC Centre for Fragment-Based Design, Monash University, Parkville, VIC 3052, Australia*

ARTICLE INFO

Keywords:
Sea anemone
Disulfide-rich peptides
Recombinant expression
NMR spectroscopy
ICK scaffold
TRPV1 channel

ABSTRACT

Sea anemone venoms are complex mixtures of biologically active compounds, including disulfide-rich peptides, some of which have found applications as research tools, and others as therapeutic leads. Our recent transcriptomic and proteomic studies of the Australian sea anemone *Telmatactis stephensoni* identified a transcript for a peptide designated Tst2. Tst2 is a 38-residue peptide showing sequence similarity to peptide toxins known to interact with a range of ion channels (Na_V, TRPV1, K_V and Ca_V). Recombinant Tst2 (rTst2, which contains an additional Gly at the N-terminus) was produced by periplasmic expression in *Escherichia coli*, enabling the production of both unlabelled and uniformly ^{13}C,^{15}N–labelled peptide for functional assays and structural studies. The LC-MS profile of the recombinant Tst2 showed a pure peak with molecular mass 6 Da less than that of the reduced form of the peptide, indicating the successful formation of three disulfide bonds from its six cysteine residues. The solution structure of rTst2 was determined using multidimensional NMR spectroscopy and revealed that rTst2 adopts an inhibitor cystine knot (ICK) structure. rTst2 was screened using various functional assays, including patch–clamp electrophysiological and cytotoxicity assays. rTst2 was inactive against voltage-gated sodium channels (Na_V) and the human voltage-gated proton (hHv1) channel. rTst2 also did not possess cytotoxic activity when assessed against *Drosophila melanogaster* flies. However, the recombinant peptide at 100 nM showed >50% inhibition of the transient receptor potential subfamily V member 1 (TRPV1) and slight (~10%) inhibition of transient receptor potential subfamily A member 1 (TRPA1). Tst2 is thus a novel ICK inhibitor of the TRPV1 channel.

1. Introduction

Sea anemones are largely sessile, predatory marine animals belonging to class Hexacorallia, one of eight venomous classes from phylum Cnidaria [1,2]. Like other members of this phylum, sea anemones possess specialised venomous cells called cnidocytes, which are distributed across various morphological structures in the body of the animals [3]. Cnidocytes are, in turn, equipped with subcellular organelles called cnidae or nematocysts, which comprise folded threads that forcibly evert to inject their venom, which plays an important role in processes such as feeding, prey capture and avoiding potential predators, all of which increase the survival of sea anemones in their habitats [1,4–10].

Sea anemones, in common with other venomous animals, produce venoms that are complex mixtures of bioactive molecules, including both non-proteinaceous (polyamines and salts) and proteinaceous components (disulfide-rich peptides and large proteins) [5,8–10]. Some of these disulfide-rich peptides are known to selectively inhibit or modulate ion channels, including voltage-gated sodium (Na_V) and potassium channels (K_V) [5,11–14]. Numerous venom-derived peptides

* Corresponding author at: Medicinal Chemistry, Monash Institute of Pharmaceutical Sciences, Monash University, 381 Royal Parade, Parkville, VIC 3052, Australia.
E-mail address: ray.norton@monash.edu (R.S. Norton).
[1] Current address: QIMR Berghofer Medical Research Institute, Brisbane, QLD, 4006, Australia.

https://doi.org/10.1016/j.bbapap.2023.140952
Received 9 May 2023; Received in revised form 15 August 2023; Accepted 25 August 2023
Available online 26 August 2023

have been approved as medications for the treatment of medical conditions such as type 2 diabetes, neuropathic pain and hypertension, whereas others are currently in clinical development [15–21]. Hence, venom-derived peptides continue to be the focus of significant interest as potential pharmacological tools and therapeutic leads [17,22,23], as well as bioinsecticides [24].

Recent progress in genomics, transcriptomics, and proteomics, together with advanced bioinformatics, has resulted in the identification of many novel peptides from sea anemones [4,25–31]. Identifying the function of these peptides, however, remains a significant challenge. While the peptide ShK [12] is a potent blocker of voltage-gated potassium channels [13], and an analogue is in clinical trials for the treatment of autoimmune diseases [19], there are many other peptides, including some in the ShKT family, that show little or no activity against a range of ion channels [32–37], and for which the endogenous function therefore remains unknown. Mass spectrometry imaging can provide clues as to the endogenous function of peptides, as exemplified by the weak K_V inhibitor Ate1a, which is produced by nematocysts and thought to be used primarily for prey capture [38].

The sea anemone *Telmatactis stephensoni* (order Actiniaria, superfamily Metridioidea) is commonly found in tropical waters of the Great Barrier Reef (Queensland, Australia) and is dangerous to humans, causing skin rashes and lesions that take weeks to heal [39,40]. These extreme reactions associated with *T. stephensoni* suggest the presence of components that are biologically active in humans, and thus provide a strong motivation for identifying new peptides in *T. stephensoni* that might show novel biological activities.

U-IPTX-Tst2, a 38 amino acid residue peptide, was identified from a recent transcriptomic and proteomic study of *T. stephensoni* [28]. The peptide was designated U-IPTX-Tst2 based on the nomenclature proposed by Oliveira et al. [41], but the truncated name Tst2 will be used here. Since Tst2 showed sequence homology (in the UniProt database [42]) with previously identified peptide toxins known to interact with ion channels such as Na_V, KCa, Ca_V and ASIC, we hypothesised that it might show similar biological activities. In this study, Tst2 was produced by recombinant periplasmic expression in *Escherichia coli*. The three-dimensional solution structure of Tst2 was determined using multi-dimensional nuclear magnetic resonance (NMR) spectroscopy and its biological activity was screened in multiple functional assays, including electrophysiological and cytotoxicity assays.

2. Materials and methods

2.1. Identification of Tst2

The peptide was found in the milked venom proteome reported by Ashwood et al. [28] (ProteomeXchange Consortium dataset PXD029717). *T. stephensoni* individuals were sourced from the Great Barrier Reef by Cairns Marine Pty Ltd. Venom was collected from *T. stephensoni* using electrical stimulation and fractionated using reversed phase high performance liquid chromatography (RP-HPLC) [28]. Subsequently, secreted venom peptides were identified from digested RP-HPLC fractions using the bottom-up proteomic approach described in [28]. Secreted venom peptide sequences containing a signal peptide were then searched against Tox-Prot database using BLASTP [43]. One of the putative venom peptides identified in the milked venom of *T. stephensoni*, Tst2, is the focus of the current study.

To localise the Tst2 peptide to a specific morphological region in *T. stephensoni*, we used the mass spectrometry imaging (MSI) protocol described previously in Surm et al. [44], with spectra of interest investigated using SCiLS Lab.

2.2. Expression and purification of recombinant Tst2 in E. coli

A codon-optimised nucleotide sequence encoding the mature peptide sequence of Tst2 was synthesised by GenScript (USA), then subcloned using BamHI and EcoR1 restriction sites into a pET21a expression plasmid (Novagen) that was previously modified by GenScript to contain the following (as shown in Fig. S1A): a MalE signal sequence to deliver the fusion protein to the *E. coli* periplasm, an N-terminal polyhistidine (His6) tag to facilitate purification using nickel (Ni)-affinity chromatography, a maltose binding protein (MBP) fusion tag (for peptide solubility), and a tobacco etch virus (TEV) protease recognition sequence (ENLYFQ) just before the peptide coding region to allow cleavage and isolation of the oxidised peptide.

2.2.1. Expression of unlabelled U-IPTX-Tst2

The plasmid containing the gene of interest was transformed into competent cells of *E. coli* strain BL21(DE3) using heat shock [45]. The cells were grown in Luria-Bertani (LB) culture medium plus 100 μg/mL of ampicillin at 37 °C and with shaking at 150 rpm until the optical density at 600 nm (OD_{600}) reached 0.8 (i.e., during the log-phase of the cell growth). 1 mM of isopropyl β-D-1-thiogalactopyranoside (IPTG, Sigma-Aldrich, MO, USA) was then added to induce expression, and the culture was incubated overnight at room temperature and 180 rpm. The culture was harvested by centrifugation for 15 min at 5000 rpm and 4 °C, and the cell pellets were stored at −80 °C.

Periplasmic expression of unlabelled Tst2 expression was also performed using an auto-induction approach. To investigate the optimal conditions for fusion protein expression via auto-induction, a starter culture was prepared by incubating the cells in LB overnight at 37 °C with 220 rpm agitation. The parent starter culture was split into four cultures (2.5 mL each) and used to inoculate four flasks each with 250 mL of the auto-induction medium ZMS-80155 [46] supplemented with 100 μg/mL ampicillin. The auto-induction medium was prepared by supplementing autoclaved LB with 1 mM $MgSO_4$, trace metals mix [46], 1 mL/L BME vitamin solution (100×; Sigma-Aldrich), 50 mM Na_2HPO_4, 50 mM K_2HPO_4, 25 mM $(NH_4)_2SO_4$, 0.5% (*w/v*) glycerol, 0.05% (w/v) glucose and 0.2% (w/v) α-lactose monohydrate. The four flasks were incubated at 37 °C with shaking at 170 rpm until an optical density (OD_{600}) of ≈ 0.8 was achieved, then the temperatures of the flasks were adjusted to 16, 25, 30 and 37 °C, and incubation continued for a further 48 h at 170 rpm. Heterologous protein expression in the four cultures was compared after 12, 24, 36 and 48 h by SDS-PAGE analysis of a cell pellet from 1 mL of each culture (normalized for cell density) to deduce the optimum conditions resulting in the highest His_6-MBP-Tst2 fusion protein expression (Fig. S1B).

2.2.2. Expression of ^{13}C, ^{15}N–labelled Tst2

For NMR structural studies, uniformly ^{13}C,^{15}N–labelled Tst2 was produced by *E. coli* expression using the dual media approach [47,48]. Cell cultures were grown in LB media supplemented with 100 μg/mL of ampicillin at 37 °C with shaking at 180 rpm, until the OD_{600} reached ≈ 0.8–1.0. The cells were harvested by spinning down in sterile centrifuge bottles for 15 min at 5000 rpm and 4 °C. The supernatant was discarded, and the cells were then resuspended in M9 minimal medium, supplemented with 2 g/L ^{13}C–glucose (Cambridge isotope laboratories [CIL], Tewksbury, MA, USA) and 1 g/L ^{15}N–ammonium chloride (CIL, Tewksbury, MA, USA) as the only carbon and nitrogen sources, respectively. The volume of M9 medium used to resuspend the cells was equivalent to one quarter of the initial LB media volume used for cell growth. The cells were grown for a further 1–1.5 h at 37 °C with shaking at 180 rpm, then induced by adding 1 mM of IPTG, and incubated overnight at room temperature with shaking at 180 rpm. The labelled culture was harvested by centrifugation for 15 min at 5000 rpm, and the cell pellets were used for purification of the labelled peptide.

2.2.3. Fusion protein purification

The His_6-MBP-Tst2 fusion protein was extracted from the *E. coli* periplasm by osmotic shock. The cell pellet was thawed for 20 min on ice to avoid lysis, then resuspended in 60 mL of 100 mM Tris, 30% sucrose, 2 mM ethylenediaminetetraacetic acid (EDTA) buffer at pH 8.0, and

incubated for 10 min at 4 °C. The suspension was centrifuged for 15 min at 4 °C and 8000 rpm, the supernatant was discarded, then the pellets were resuspended in 60 mL of ice-cold water and 5 mM $MgCl_2$ ($MgCl_2$ is to protect the inner cell membrane from lysis) and incubated for a further 10 min at 4 °C before centrifugation for 15 min at 4 °C and 16,000 rpm. The supernatant (periplasmic extract) containing soluble His_6-MBP-Tst2 fusion protein was diluted in 20 mM Tris, 150 mM NaCl, 5% glycerol, pH 7.5 (TNG buffer) and incubated for 30 min with 5 mL Ni-nitrilotriacetic acid (Ni-NTA) Fast Flow resin (GE Healthcare, Uppsala, Sweden) in a gravity-fed column to capture the fusion protein via its affinity to Ni-NTA. Then, 25 mM imidazole was used for washing the resin to facilitate the removal of non-specifically bound proteins. The His_6-MBP-Tst2 fusion protein was eluted with a 100–400 mM imidazole gradient and the fractions containing the fusion protein (as assessed by SDS-PAGE) (Fig. S2) were concentrated by centrifugal filtration (Amicon® Ultra, Millipore). Imidazole was removed from the concentrated sample using a PD-10 column (GE Healthcare, Pittsburg, PA, USA). Fig. S3 shows a schematic representation of Tst2 periplasmic expression in *E. coli* and His_6-MBP-Tst2 fusion protein purification.

2.2.4. TEV cleavage and removal of the cleaved His_6-MBP and His_6-TEV protease

TEV protease was able to cleave the His_6-MBP-Tst2 fusion protein without the addition of thiol reagents, which had the advantage of minimising potential shuffling of the pre-formed disulfide bonds in the peptide. Note that TEV cleavage leaves an additional Gly residue at the N-terminus of the recombinant peptide, which is designated Gly-1 to distinguish it from the native N-terminal residue Cys1; this peptide will be referred to as rTst2 to distinguish it from the native peptide. SDS-PAGE was used to monitor fusion protein cleavage (Fig. S4). The cleavage mixture was then passed over Ni-NTA Fast Flow resin to remove the cleaved His_6-MBP and His_6-TEV protease, and the eluate containing the cleaved rTst2 was collected for further purification by RP-HPLC.

2.2.5. RP-HPLC purification and LC–MS analysis

RP-HPLC purification was performed on a Vydac C18 column (300 Å, 10 μm, 250 × 10 mm) using a flow rate of 4 mL/min and a gradient of 0%–100% solvent B (0.1% trifluoroacetic acid (TFA) in 90% acetonitrile) in solvent A (0.1% TFA in water) over 60 min, with absorbance monitored at 214 nm. Fractions corresponding to rTst2 were collected and assessed by liquid chromatography–mass spectrometry (LC-MS). Fractions containing pure rTst2 (>99%) with the correct molecular mass (4022.68 Da) were lyophilised for NMR structural studies and functional assays.

2.3. NMR spectroscopy

The rTst2 sample for NMR experiments was prepared by dissolving lyophilised peptide at a final concentration of 0.55 mM in 90% H_2O/10% ^2H_2O, and the pH was adjusted to 4.7. For deuterium exchange experiments, a lyophilised sample of rTst2 (whose pH had been pre-adjusted to 4.7 in H_2O) was dissolved in 100% ^2H_2O at a concentration of 0.55 mM.

NMR spectra were recorded at 20 °C using a Bruker 600 MHz spectrometer (Billerica, MA, USA) equipped with a cryogenically cooled TCI probe. Multidimensional heteronuclear NMR spectra were obtained on a uniformly ^{13}C,^{15}N–labelled sample of rTst2 for establishing the backbone and sidechain resonance assignments. The acquired NMR spectra included: One-dimensional (1D) ^1H, two-dimensional (2D) [^1H—^1H] total correlation spectroscopy (TOCSY), 2D [^1H–^1H] nuclear Overhauser effect spectroscopy (NOESY), 2D double quantum filtered correlation spectroscopy (DQF-COSY), 2D ^1H—^{15}N (heteronuclear single quantum coherence) HSQC, 2D ^1H—^{13}C HSQC, 3D HNCACB, 3D CBCA(*CO*)NH, 3D HNCO, 3D CC(*CO*)NH and ^{15}N-edited NOESY-HSQC. NMR spectra were acquired using either conventional or non–uniform sampling (NUS) in order to reduce the data acquisition time [49]. Conventional NMR spectra were processed using Bruker TopSpin (version 3.6.3), and NUS spectra were constructed using the maximum entropy (MaxEnt) algorithm [50] and processed using NMRpipe [51], which is available via the NMRbox platform [52]. Resonance assignments were made using NMRFAM-Sparky Analysis (Version 3.134) [53]. 1,4-dioxane was used as a chemical shift reference in the ^1H dimension by calibrating the 1,4-dioxane methylene peaks to 3.75 ppm, with the ^{13}C and ^{15}N dimensions being calibrated indirectly. Table S1 shows further details of the whole set of NMR experiments used for Tst2 structure calculations, and their acquisition parameters.

For the pH titration, a set of 1D ^1H NMR spectra of rTst2 was acquired over the pH range 2–7. A further set of 1D ^1H NMR spectra was recorded over the temperature range 5–30 °C in increments of 5 °C for determination of the temperature coefficients of the amide protons in order to detect potential hydrogen bond donors [54]. Exchange of the amide protons with deuterium was monitored by the acquisition of a series of 1D ^1H and 2D TOCSY spectra at 5 °C immediately after dissolution of the lyophilised peptide in 100% ^2H_2O.

2.4. Calculation of rTst2 structure

The structure of rTst2 was calculated using experimentally generated distance restraints derived from intensities of NOEs in 2D NOESY and ^{15}N–edited NOESY spectra. In total, 691 NOE-derived distances were converted into unambiguous structural restraints. The $^3J_{HNH\alpha}$ scalar coupling constants measured from 1D ^1H or DQF-COSY spectra were used to determine the dihedral (torsion) angle constraints, using the following ranges: φ $-120 \pm 40°$ when $^3J_{HNH\alpha} \geq 8$ Hz and $-65 \pm 25°$ when $^3J_{HNH\alpha} \leq 6$ Hz [55]. Initial structures were calculated without defining the three disulfide bonds in order to define the disulfide connectivities according to the proximity of Cys SH groups and NOEs between Hβs of Cys residues, which were then used as constraints in the subsequent rTst2 structure calculations. Three distance restraints were used for disulfide connectivity as follows: 2, 3 and 3 Å for S(i)-S(j), S(i)–Cβ(j), and S(j)–Cβ(i), respectively. Amino acid residues involved in hydrogen bonds were predicted from amide proton exchange rates and temperature coefficients [54], and were included as restraints in subsequent structure calculations. All of these restraints were used to calculate the structure of rTst2 using CYANA (version 3.98.13) [56]. CYANA generated an ensemble of 100 structures of rTst2, from which the 20 structures with the lowest energy values were selected for structure analysis. The structures generated using CYANA were refined by simulated annealing, first in vacuo, then in implicit solvent using the EEFx force field in XPLOR-NIH (version 2.48) [57]. All the figures of rTst2 structure were generated using PyMOL. (http://www.pymol.org).

2.5. Electrophysiological assays

Chinese hamster ovary (CHO) cells (American Type Culture Collection) were grown in DMEM-high glucose supplemented with 10% foetal bovine serum, 2 mM L-glutamine, 100 μg/mL penicillin-g, and 100 μg/mL streptomycin (Invitrogen, Carlsbad, CA, USA) at 37 °C in a 5% CO_2 and 95% air humidified atmosphere. Cells were passaged twice per week following a 7-min incubation in phosphate-buffered saline containing 0.2 g/L trypsin-EDTA (Invitrogen).

CHO cells were transiently transfected with plasmids encoding $hK_V2.1$, $hNa_V1.3$, $hNa_V1.5$, $hNa_V1.7$, hTRPA1, or hH_V1 using Lipofectamine 2000 (Invitrogen) following the manufacturer's protocol, then cultured under standard conditions. The cells were co-transfected with a plasmid encoding green fluorescent protein (GFP) at a molar ratio of 10:1 except for $hNa_V1.5$ for which a GFP-tagged ion channel vector was used. GFP-positive transfectants were identified with a Nikon Eclipse TS100 fluorescence microscope (Nikon, Tokyo, Japan) using bandpass filters of 455–495 nm and 515–555 nm for excitation and emission, respectively, and these cells were used for current recordings (>70%

success rate for transfection). Human embryonic kidney (HEK) 293 cells stably expressing $hNa_V1.4$ were used. hTRPV1 channels were expressed in a stable manner in CHO cells. Cells were washed gently twice with 2 mL of extracellular solution (ECS, see below) and re-plated onto 35-mm polystyrene cell culture dishes (Cellstar, Greiner Bio-One) for the patch-clamp experiments. In general, ionic currents were recorded 24–36 h after transfection.

Standard whole-cell patch-clamp electrophysiology method [58] was used for recording ionic currents. Micropipettes were pulled in four stages using a Flaming Brown automatic pipette puller (Sutter Instruments, San Rafael, CA, USA) from GC 150F-15 borosilicate glass capillaries (Harvard Apparatus Co., Holliston, MA, USA) with tip diameters of 0.5–1 μm, and heat polished to a tip resistance of typically 2–8 MΩ. All measurements were carried out by using Axopatch 200B amplifier connected to a personal computer using Axon Digidata 1550A data acquisition hardware (Molecular Devices, Sunnyvale, CA, USA). Current records were discarded when leak at the holding potential was >10% of peak current at the given test potential. For Na^+ current recordings, series resistance compensation up to 70% was used to minimise voltage errors and achieve proper voltage-clamp conditions. Experiments were performed at room temperature (20–24 °C). Data were analysed with GraphPad Prism 8 (GraphPad, CA, USA) and ClampFit 10.5 (Molecular Devices Inc., Sunnyvale, CA, USA). Before analysis, whole-cell current traces were digitally filtered with a three-point boxcar smoothing filter. For hH_V1, hTRPA1, and hTRPV1 only those currents were analysed for which the reversal potential fell into the range of the theoretical reversal potential ±5 mV (−72.8 ± 5 mV for hH_V1, and 0 ± 5 mV for hTRPA1 and hTRPV1).

All salts and components of the solutions were purchased from Sigma Aldrich, Budapest, Hungary. For $hK_V2.1$, $hNa_V1.3$, $hNa_V1.4$, $hNa_V1.5$ and $hNa_V1.7$ the extracellular (bath) solution (ECS) contained 145 mM NaCl, 5 mM KCl, 2.5 mM $CaCl_2$, 1 mM $MgCl_2$, 10 mM HEPES and 5.5 mM glucose (pH 7.35 with NaOH). For $K_V2.1$, the intracellular (pipette) solution (ICS) contained 140 mM KF, 2 mM $MgCl_2$, 1 mM $CaCl_2$, 11 mM EGTA and 10 mM HEPES (pH 7.22 with KOH). For recordings of Na^+ currents, the composition of ICS was 105 mM CsF, 10 mM NaCl, 10 mM EGTA and 10 mM HEPES, (pH 7.2 with CsOH). For hH_V1 (in mM) 60 L-Asp with Na, 80 MES, 5.5 glucose, 6 $MgCl_2$ (pH 7.4 with CsOH) and an ICS of (in mM) 90 L-Asp with Na, 80 MES, 6 $MgCl_2$, 3.3 glucose (pH 6.4 with CsOH). For recordings of TRPA1 and TRPV1 currents, the ECS and ICS contained 150 mM NaCl, 2 mM Na-EDTA and 10 mM HEPES (pH 7.35 with NaOH). The osmolarity of the ECS and ICS were 302–308 mOsM and ~ 295 mOsM, respectively. Solutions containing rTst2 were made fresh in ECS supplemented with 0.1 mg/mL bovine serum albumin (BSA, Sigma-Aldrich Hungary, Budapest, Hungary) from 100 mM stocks stored at −20 °C. Positive controls were applied at a concentration approximately equivalent to their IC_{50} values: 10 mM TEA^+ for $K_V2.1$, 200 μM 5-chloro-2-guanidinobenzimidazole (ClGBI, Sigma-Aldrich, Hungary) for hH_V1, 50 μM HC-030031 for TRPA1, and 50 μM capsazepine for TRPV1, respectively. For Na_V channels a choline-based ECS was used as control, whose composition was (in mM) 145 choline-Cl, 5 KCl, 10 Hepes, 5.5 glucose, 2.5 $CaCl_2$ and 1 $MgCl_2$. Bath perfusion around the measured cell with different extracellular solutions was achieved using a gravity flow micro perfusion system at a rate of 200 μL/min. Excess fluid was removed continuously. The approximately 50% reduction in the current amplitude in the presence of the positive controls or a prominent change in the current kinetics (i.e., complete reduction of the sodium current in a choline-based ECS) were an indicator of both ion channel integrity and the proper operation of the perfusion system.

For measurement of $hK_V2.1$ current, 50-ms-long voltage steps to +50 mV were applied from a holding potential of −120 mV every 15 s and the peak current was measured. For Na^+ current recordings, 10-ms-long voltage steps from a holding potential of −120 mV to 0 mV were applied every 10 s. Current through hH_V1 was elicited every 10 s with voltage ramps to +60 mV from −60 mV at a rate of 0.12 mV/ms. hTRPA1 and hTRPV1 currents were elicited every 5 s with 200-ms-long voltage ramps −50 mV to +50 mV. The cells were held at 0 mV during the subsequent pulses. TRPA1 and TRPV1 currents were activated by 100 μM allyl-isothiocyanate (AITC) and 1 μM capsaicin, respectively. The remaining current fraction (RCF) at a given molar concentration was calculated as I/I_0, where I_0 is the peak current in the absence, and I is the peak current in the presence of rTst2 at equilibrium block or in the absence of inhibition after ~2 min perfusion with rTst2.

2.6. Injection assay in Drosophila melanogaster

rTst2 activity in *Drosophila melanogaster* was assessed using an injection activity assay described previously [59]. The mass of female *D. melanogaster* used for this experiment ranged from 0.8 to 1.1 mg. Five doses of Tst2 (0.00005, 0.0005, 0.005, 0.05 and 0.5 μg per fly) were each administered to eight *D. melanogaster* (n total = 40), and paralysis and mortality were monitored at 2 and 24 h post-injection. Dose-response data were analysed as described previously [59]. Eight *D. melanogaster* were used as an injection control group and administered 50 nL of water.

3. Results

3.1. Identification of Tst2

The precursor of Tst2 is an 84-residue peptide identified in *Telmatactis stephensoni*. This putative venom peptide has a signal peptide of 25 amino acid residues (MVQMKGFGILCLVFLVVFLMNVAES), a propeptide of 21 amino acid residues (RRYPEFPMPYNDDYDKPFVKR) and mature peptide of 38 amino acids residues with 6 cysteines (CKGQDAPCSKSKDCCGEASMCSKGADGKKTCMIDKLWG) (Fig. 1). The mature amino acid sequence of Tst2 has a predicted molecular mass of 3965.59 Da, assuming the six cysteines form three disulfide bridges. MALDI-MSI showed that a spectral peak (3968.03 m/z ± 1.13 Da) close to the expected mass of the peptide was not localised to a particular morphological structure in the sea anemone (Fig. 2). Slightly higher expression of Tst2 was observed in the epidermis structures (column and pedal disc) (data not shown), consistent with this peptide having a role in predator deterrence in *T. stephensoni* [4].

A sequence similarity search against UniProtKB_SwissProt database using BLASTP 2.12.0+ [60] revealed that mature Tst2 sequence shares 42.2% sequence similarity (E-value = 2.73×10^{-4}) with a voltage-gated sodium channel inhibitory (Na_V) toxin U2-ctenitoxin-Pn1a (P29423) from the Brazilian armed spider *Phoneutria nigriventer* [61]. A multiple sequence alignment of the mature Tst2 peptide with sequences with significant similarity (E-value <0.05) is shown in Fig. 3.

3.2. Recombinant expression and purification of His_6-MBP-Tst2 fusion protein

Periplasmic expression of Tst2 in *E. coli* was used in order to facilitate native disulfide formation without the need for subsequent oxidative folding in vitro. The His_6-MBP-Tst2 fusion protein was the dominant protein expressed following IPTG/auto-induction (lane 2 in Fig. S2). His_6-MBP-Tst2 fusion protein was extracted from the periplasmic space by osmotic shock in 5 mM $MgCl_2$ and purified using immobilised metal affinity chromatography (IMAC) by passing over Ni-NTA Fast Flow resin to purify the peptide from the His_6-tagged MBP. The majority of the His_6-tagged MBP fusion protein was eluted in the 200 and 300 mM imidazole fractions of the eluting imidazole gradient (100–400 mM imidazole) (Fig. S2). A PD-10 gravity flow desalting column packed with Sephadex G-25 resin was used to remove imidazole from the samples.

3.3. Optimisation of the yield of recombinant Tst2

The periplasmic expression of rTst2 in *E. coli* via IPTG induction yielded approximately 0.4–0.5 mg of soluble peptide per liter of culture.

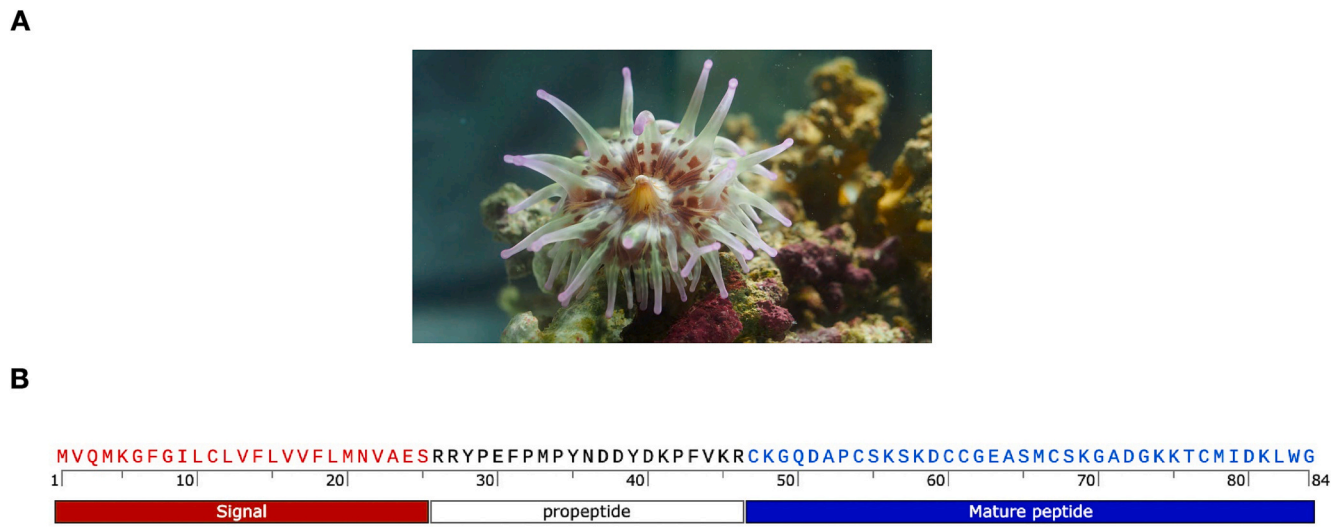

Fig. 1. Identification of Tst2 peptide in the sea anemone *Telmatactis stephensoni*. A. *T. stephensoni* individual. B. Full-length amino acid sequence of the Tst2 peptide. Signal peptide highlighted in black, propeptide in grey, mature peptide in blue. (For interpretation of the references to colour in this figure legend, the reader is referred to the web version of this article.)

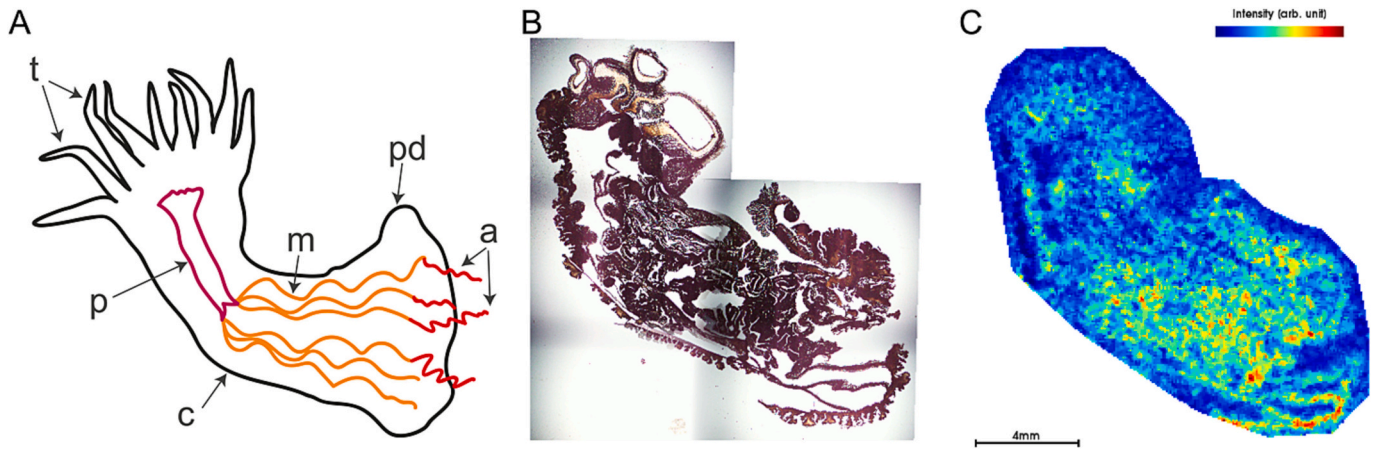

Fig. 2. Localisation and abundance of the Tst2 peptide across morphological structures of *Telmatactis stephensoni*. A. Schematic of the envenoming morphological structures. B. Haematoxylin and eosin-stained longitudinal section. C. Mass spectrometry imaging (MSI) data showing that a putative peptide observed at 3968 *m/z* (± 1.13 Da) is not localised to a particular morphological structure. c = club-tips, t = tentacles, p = pharynx, b = body column, m = mesenterial filaments, pd = pedal disc, a = acontia.

Peptide	Sequence	aa	%Similarity
U-IPTX-Tst2	**---CKGQDAPCSKSKDCCGEASMCSKGA--DGKKTCMID--KLWG----------**	**38**	
P29423; U2-ctenitoxin-Pn1a; *Phoneutria nigriventer*; Nav.....	-ATCAGQDKPCKETCDCCGERGECVCALSYEGKYRCICRQGNFLIAWHKLASCK------	53	42.2
P84012; U7-ctenitoxin-Pk1a; *Phoneutria keyserlingi*; Nav.....	-ATCAGQDKPCKETCDCCGERGECVCGLSYEGKYRCICRQGTFLIAWYKLASCKK-----	54	39.6
P83904; Delta-ctenitoxin-Pr2d; *Phoneutria reidyi*; Nav.....	-GTCAGQDKPCKETCDCCGERGQCVCEG------PCICRQGYFWIAAYKLGNCK------	47	38.8
O76198; U2-ctenitoxin-Pn1b; *Phoneutria nigriventer*; Nav.....	-ATCAGQDKPCKETCDCCGERGECVCALSYEGKYRCICRQGYVWIAWYKLASCK------	53	39.6
P85275; U8-ctenitoxin-Co1a; *Ctenus ornatus*; Nav.....	DGKCAGQDKPCKNSCDCCGARGECVYTGYXP----------	31	37.0
P29425; Delta-ctenitoxin-Pn2a; *Phoneutria nigriventer*; Nav.....	-ATCAGQDQPCKETCDCCGERGECVCGG------PCICRQGYFWIAWYKLANCKK-----	48	38.8
P85276; U5-ctenitoxin-Co1a; *Ctenus ornatus*; Nav.....	TATCAGQDKPCQKHCDCCGPKGECVCEG------PCICRQG----------	35	36.2
P60976; U1-nemetoxin-Csp1a; *Calisoga sp*.....	---CISARYPCSNSKDCCSGN----------CGTFWTCYIRKDPCSKECLAP	39	37.0
P84028; Delta-ctenitoxin-Asp2e; *Ancylometes* sp.; Nav.....	-ATCAGQDKPCKVNCDCCGERGECVCGG------PCICRQGNVFIAWSKLMTCK------	47	35.7
	* . ** . *** .		

Fig. 3. Amino acid sequence alignments of Tst2 peptide. Peptides with sequence similarity were identified by searching against UniProtKB_SwissProt database using BLASTP 2.12.0+. Sequences used in the alignment are indicated by UNIPROT ID, short name, source organism and ion channel targeted. Residues identical to Tst2 main chain sequence are bolded in black. Cysteine residues shared with Tst2 peptide are bolded in blue, additional cysteine residues are bolded in red. Sequence alignment was performed using Clustal Omega (v.1.2.4, https://www.ebi.ac.uk/Tools/msa/clustalo/, accessed in December 2022) [62–64]. * indicates conserved amino acid residues in all peptide toxins. (For interpretation of the references to colour in this figure legend, the reader is referred to the web version of this article.)

In an attempt to achieve a higher yield of unlabelled rTst2, the auto-induction approach was used to express the His_6-MBP-Tst2 fusion protein. An initial expression experiment was performed on a small scale of culture (4 × 250 mL mini cultures) to determine the optimum cell growth conditions used in subsequent cultures. When the optical density (OD_{600}) of the cultures reached ≈ 0.8, the temperatures of the flasks were adjusted to 16, 25, 30 and 37 °C, and allowed to proceed over 48 h at 170 rpm. By comparing the His_6-MBP-Tst2 fusion protein expression in the four cultures over 48 h in 12 h time points, it was observed that culture at 25 °C after 36 h produced the most intense fusion protein band on SDS-PAGE (Fig. S1B), and the final yield of soluble peptide was 0.9 mg/L of cell culture, whereas the yield of soluble peptide was 0.6 mg/L, 0.7 mg/L and 0.3 mg/L at 16, 30 and 37 °C respectively. Hence, auto-induction at 25 °C was used in subsequent cultures to express unlabelled rTst2.

3.4. RP-HPLC purification of Tst2 and verification of the identity and purity with LC-MS

rTst2 was purified using RP-HPLC, and a major peak was eluted at 34.38 min (equivalent to 31% solvent B) using a 60 min linear gradient of 0–100% solvent B (0.1% TFA in acetonitrile) (Fig. S5). The fractions corresponding to the rTst2 peak were analysed by LC-MS to check purity and identity. The LC-MS profile displayed a single pure peak with a molecular mass (MH^+ m/z = 4022.7 Da) that is 6 Da less than that of the predicted mass of the reduced form of rTst2 (MH^+ m/z = 4028.67 Da) and closely matching the expected mass of the oxidised peptide (theoretical MH^+ m/z = 4022.68 Da) (Fig. S6A), thus confirming formation of three disulfide bonds. This molecular mass (MH^+ m/z = 4022.7 Da) corresponds to the oxidised form of rTst2 following cleavage with TEV protease, which includes a residual glycine from the TEV cleavage site at the N-terminus of the recombinant peptide. Similarly, a major pure peak was observed in the LC-MS profile of the oxidised form of the uniformly ^{13}C,^{15}N–labelled rTst2 (Fig. S6B) after being purified by RP-HPLC.

3.5. NMR spectroscopy and sequence-specific resonance assignments of rTst2

The 1D ^1H NMR spectrum of rTst2 at pH 4.7 and 20 °C (Fig. 4A), showed that rTst2 exhibited well dispersed sharp peaks in the amide region with narrow line widths (Fig. 4B), indicating that the recombinant Tst2 adopted a single major conformation with a well-defined tertiary structure.

A pH titration was performed using 1D ^1H NMR spectra acquired over the pH range 2–7 (Fig. S7). Above pH 5, some amide protons started to show peak broadening owing to exchange with the solvent (90% H_2O/10% ^2H_2O) [65]. Initially, therefore, all spectra used for sequential assignments were recorded at pH 5 and 20 °C, but after partial assignments had been performed, it was observed that cross-peaks from Asp5 and Ser11 were overlapping as shown in the 2D ^1H—^{15}N HSQC (Fig. S8A), whereas at pH 4.7 they were well resolved (Fig. S8B), so subsequent spectra were recorded at pH 4.7 and 20 °C. Sequential

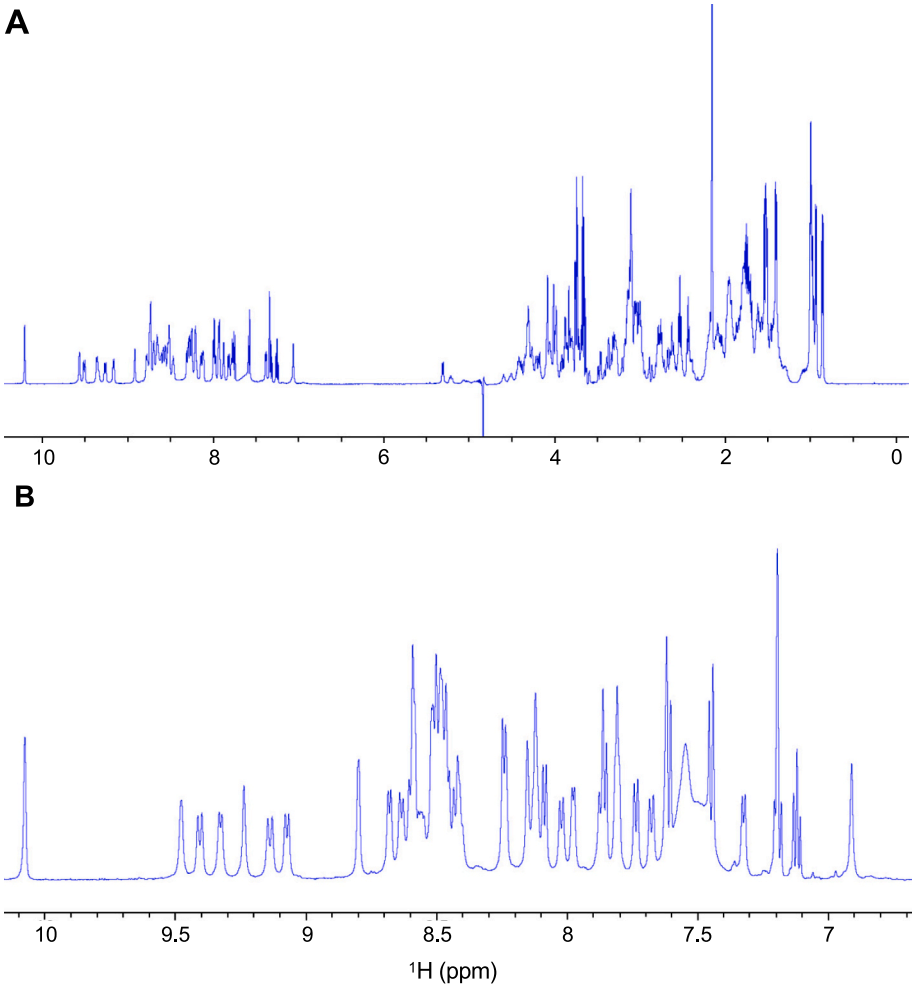

Fig. 4. 1D ^1H NMR spectrum of rTst2 in 90% H_2O/10% ^2H_2O, acquired on a Bruker 600 MHz NMR spectrometer at pH 4.7 and 20 °C. A. Full spectrum of rTst2. B. Expanded amide/aromatic region.

backbone and side chain resonance assignments of rTst2 were performed utilising 2D and 3D NMR spectra acquired on 0.5 mM unlabelled and 0.55 mM $^{13}C—^{15}N$ labelled peptide samples, respectively, as follows: 2D [$^{1}H–^{1}H$] TOCSY, 2D [$^{1}H–^{1}H$] NOESY, 2D [$^{1}H–^{1}H$] DQF-COSY, 2D [$^{1}H–^{15}N$] HSQC, 3D HNCACB, 3D CBCA(*CO*)NH, 3D HNCO, 3D CC(*CO*)NH and ^{15}N–edited NOESY–HSQC. Examples of assignment strip plots from 3D HNCACB and 3D CBCA(*CO*)NH spectra are shown in Fig. S9. 2D DQF-COSY and TOCSY spectra were used for side-chain assignments, while stereospecific resonance assignments were obtained from 2D NOESY and ^{15}N–edited NOESY–HSQC spectra.

Table S2 displays the ^{1}H, ^{15}N and ^{13}C chemical shifts of rTst2, which have been deposited in BioMagResBank [66] (BMRB id 51901). A fully assigned 2D [$^{15}N–^{1}H$]–HSQC spectrum with backbone and sidechain resonance assignments is shown in Fig. 5. Cross peaks for the backbone correlations in the [$^{15}N—^{1}H$]–HSQC were observed for all amino acid residues except for the N-terminal Gly-1 and Pro7. A total of 40 cross peaks was observed in the [$^{15}N—^{1}H$]–HSQC spectrum; 37 backbone correlations, Gln4 side chain (two) and one Trp37 indole NH.

3.6. rTst2 disulfide bond connectivity

The LC-MS data for rTst2 confirmed that all six cysteine residues were involved in three disulfide bonds (Fig. S6). Moreover, the Cα and Cβ chemical shifts of the six cysteines were in the ranges of 53.5–56.2 ppm and 39.2–47.0 ppm, respectively (Fig. S10), consistent with oxidised Cys residues [67]. The rTst2 disulfide bond connectivity was unequivocally determined from preliminary structure calculations calculated by CYANA using NOE distance restraints without defining disulfide connectivities [68]. The disulfide connectivities Cys1-Cys15, Cys8-Cys21, and Cys14-Cys31 were identified based on the proximity of Cys residues and were consistent with NOEs between Hβ resonances of Cys residues. These connectivities were used as restraints in the subsequent rTst2 structure calculations.

3.7. Three-dimensional structure of rTst2

The rTst2 structure calculations were performed by CYANA using 691 NOE-derived distance restraints derived from NOESY spectra recorded at 600 MHz, eight dihedral angle restraints, seven hydrogen-bond restraints derived from deuterium exchange experiment, and nine disulfide bond restraints, resulting in a total of 715 restraints (corresponding to an average of 18.3 restraints per residue). Slowly exchanging amide protons observed 1 h and 8 h after dissolution of unlabelled rTst2 sample in 100% $^{2}H_2O$ (Fig. S11) and having temperature coefficients less negative than −4.6 ppb/K (Table S3) were included as hydrogen-bond constraints in structure calculations. rTst2 structural constraints and statistics are summarised in Table 1.

Fig. 6A shows a stereo view of the final ensemble of 20 lowest energy structures from 100 initial structures calculated by CYANA. Fig. 6B displays a stereo view of the closest-to-average structure of rTst2 highlighting the disulfide bonds and the key secondary structure elements.

Table 1
Summary of NMR restraints and structure statistics for rTst2.

NMR distance and dihedral constraints	
Total NOEs	691
Intra-residue	333
Inter-residue	
Sequential	175
Medium-range	52
Long-range	131
Disulfide bond restraints	9
Hydrogen bond(s)	7
Dihedral angles	
Backbone (φ angle)	8
Structure statistics	
RMSD between 20 conformers (Å)	
Average pairwise RMSD (Å)	
All backbone atoms (Å) (N, Cα, C)	0.7 ± 0.25
All heavy atoms (Å)	1.06 ± 0.2
Backbone atoms (Residues 1–14, 19–23, 27–34)	0.29 ± 0.06
Heavy atoms (Residues 1–14, 19–23, 27–34)	0.77 ± 0.12
Ramachandran analysis	
Residues in most favoured regions (%)	60.9
Residues in additionally allowed regions (%)	38.9
Residues in generously allowed regions (%)	0.2
Residues in disallowed regions (%)	0.0

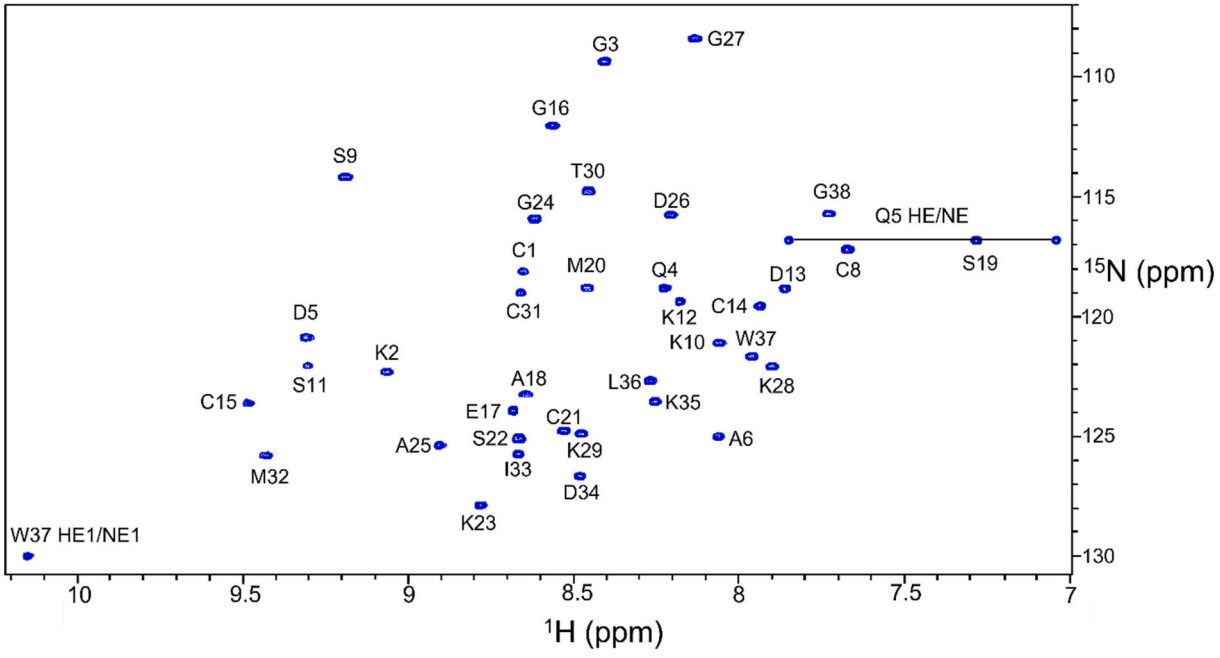

Fig. 5. Two-dimensional [$^{1}H—^{15}N$]-HSQC spectrum of rTst2 with resonance assignments. The spectrum was acquired at pH 4.7 and 20 °C on a Bruker Avance III 600 MHz spectrometer. A horizontal line connects the Gln4 side chain amide cross-peaks.

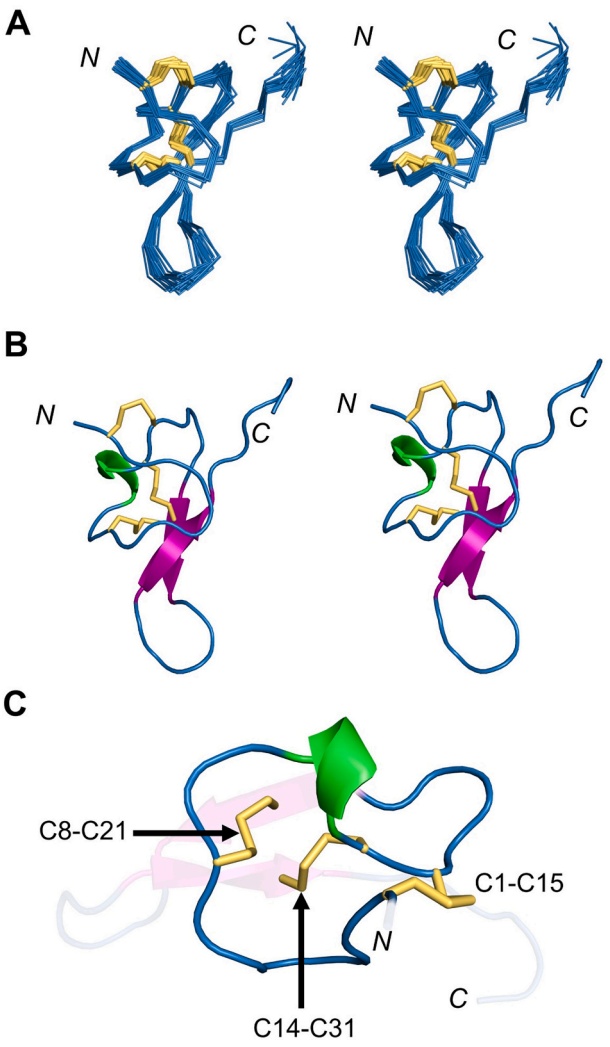

Fig. 6. A. Stereo view (cross-eyed) of the best 20 converged structures of rTst2, superimposed over the backbone heavy atoms N, Cα and carbonyl carbon for amino acid residues 1–38, with disulfide bonds shown as yellow sticks. B. Stereo view (cross-eyed) of a cartoon representation of the closest to average structure of rTst2. The two antiparallel β-strands are shown in magenta, while the single turn of 3_{10}-helix is colored in green. *N* and *C* indicate N– and C–termini, respectively. Numbers indicate the positions of Cys residues. C. The closest-to-average rTst2 structure is rotated such that the ICK motif [69,70] is clearly visible. The ICK ring (shown in blue) is formed by two disulfide bonds (Cys1-Cys15 and Cys8-Cys21) and the third ICK disulfide bond (Cys14-Cys31) passing through this ring. (For interpretation of the references to colour in this figure legend, the reader is referred to the web version of this article.)

While the Cys1-Cys15 disulfide bond is likely to be critical in maintaining the high degree of order at the N-terminus of rTst2, the C-terminal region is flexible, leading to a high overall backbone atom root-mean-square deviation (RMSD) of 0.7 ± 0.25 Å. The backbone RMSD is much lower (0.29 ± 0.06 Å) for the relatively rigid regions (residues 1–14, 19–23 and 27–34).

The structure consists of a hairpin motif formed by two antiparallel β-strands encompassing amino acid residues 20–23 and 29–32. This was evidenced by the large $^{3}J_{HNH\alpha}$ (≥ 8 Hz) coupling constants (e.g. Met20, Cys21, Lys29 and Met32), strong sequential *d*αN, inter-strand NH-NH (e.g. Ser22 NH-Thr30 NH, Met32 NH-Met20 NH and Met32 NH-Ser22 NH [Fig. S12]) and NH-CαH connectivities, and slowly exchanging amide protons (e.g. Met20, Ser22, Thr30, Cys31, and Met32 [Fig. S11]). The two antiparallel β-strands are linked by a hairpin loop (Gly24, Ala25, Asp26, Gly27 and Lys28). Additionally, residues 11–13 form a single turn of 3_{10}-helix (α1). The Ala6-Pro7 peptide was assigned as *trans* based on the strong $d_{\alpha\delta}$ NOEs between Ala6 and Pro7 (Fig. S13A). Furthermore, the chemical shift difference between the Pro7 Cβ and Cγ resonances (Δβγ) is <5 ppm (4.6 ppm), supporting the *trans*-conformation of the Ala6-Pro7 peptide bond (Fig. S13B) [71]. The final structures of rTst2 have been deposited in the Protein Data Bank [72] with id 8SEM.

In common with many disulfide-rich peptides, the disulfide themselves make up the core of the rTst2 structure, which therefore lacks a significant hydrophobic core. The side chain of Ile33 is largely buried and could be considered part of the core, but Met20 is exposed to solvent and close in space to Met32 (Fig. 7). Leu36 and Trp37 form a small hydrophobic cluster at the C-terminus (Fig. 7A, B). The loop encompassing residues 23–29 is highly charged, with three Lys and Asp26. As shown in Fig. 7C and 7D, there is an uneven distribution of charge on the surface of the peptide, with one face being largely negatively charged and the opposite face largely positive; it would be of interest to investigate the functional significance of this charge distribution in future studies.

A search for structural homologues in Dali [74] revealed that rTst2 has similar topology to several peptide toxins having the ICK scaffold (Fig. 8). The rTst2 structural homologues are ω-atracotoxin (ACTX)-HVI, hainantoxin-III (HNTX-III) and tachystatin B1. ω-atracotoxin (ACTX)-HVI (PDB; 1AXH), a 37 amino acid residue peptide isolated from the Blue Mountains funnel web spider *Hadronyche versuta*, inhibits an insect voltage-gated calcium channel [75]. Hainantoxin-III (HNTX-III, PDB; 2JTB), a 33 amino acid residue peptide isolated from the venom of the spider *Ornithoctonus hainanaz*, is a selective antagonist of neuronal tetrodotoxin-sensitive voltage gated sodium channels [76]. Tachystatin B1 (PDB; 2DCV), an antimicrobial ICK-containing peptide with 42 amino acid residues, was isolated from the Japanese horseshoe crab *Tachypleus tridentatus* [77].

3.8. Functional assays

Guided by the structural homologies documented above, rTst2 was tested against voltage-gated potassium, sodium and proton channels. Whole-cell currents were recorded sequentially on the same transiently or stably transfected CHO cell, before (control, black) and after perfusion of the cell with 100 nM rTst2 (red) (Fig. 9A). We observed slight potentiation of the hKv2.1 current: at equilibrium, rTst2 caused a ~ 10% increment in current amplitude. This weak potentiation, which did not modify the activation kinetics of the channel (data not shown), was almost fully reversible upon washing the perfusion chamber with rTst2-free solution. Interestingly, the observed effect did not show concentration dependence: RCF values were 1.1 ± 0.03 at 100 nM ($n = 5$), and 1.1 ± 0.04 at 1 μM ($n = 4$), respectively. rTst2 was also tested against the voltage-gated sodium channels $Na_V1.3$, $Na_V1.4$, $Na_V1.5$, and $Na_V1.7$, but none was inhibited significantly by rTst2 at 100 nM (Fig. 9B-E).

The voltage-gated proton channel (H_V1) is a relatively recently identified ion channel that differs structurally from most voltage-gated ion channels due to the lack of a pore domain. At 100 nM, rTst2 neither inhibited H_V1 nor interfered with activation gating of the channel (Fig. 9F).

As *T. stephensoni* can cause painful stings and skin rashes, rTst2 was also tested against channels involved in pain recognition, such as the transient receptor potential channels TRPA1 and TRPV1 (Fig. 9G, H). TRPA1 and TRPV1 channels were activated by 100 μM AITC and 1 μM capsaicin, respectively, then rTst2 was added after complete activation of the current. We found that TRPA1 was only slightly inhibited by rTst2 at 100 nM (by ~10%, RCF was 0.92 ± 0.01, n = 4), but a prominent inhibition was observed for the TRPV1 current: at equilibrium inhibition, 100 nM Tst2 caused >50% reduction in current amplitude (RCF was 0.48 ± 0.08, n = 4) (Fig. 9H, I). The block was partially reversible; after 6 min wash-out the current amplitude was ~80% of the control.

rTst2 was also assayed for insecticidal activity by being injected in a dose of 0.5 μg/fly into *D. melanogaster*, but there were no signs of

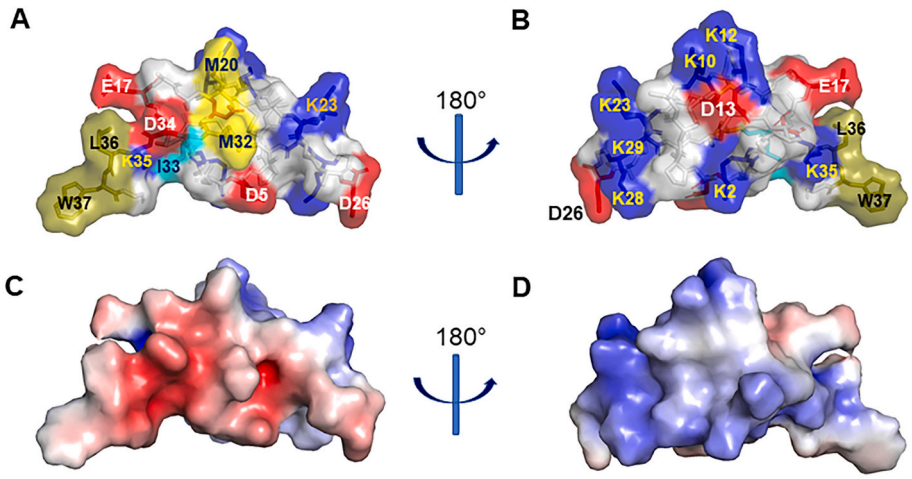

Fig. 7. Surface representation of rTst2. The two views in A and B (obtained by a 180° rotation on the indicated axis) show the surface exposure of the key amino acid residues. Leu36 and Trp37 (forming the hydrophobic cluster) are green olive, Met20 and Met32 are yellow, Ile33 is cyan, and basic and acidic residues are blue and red, respectively. The remaining amino acid residues are shown in light grey. C and D are two views of the electrostatic potential map of rTst2 at 180° rotation around its longitudinal axis. The rTst2 electrostatic potential map was calculated with Adaptive Poisson-Boltzmann Solver (APBS) [73] and mapped onto the solvent-accessible surface of the molecule, at contouring levels of ±5 kT/e (blue/red). (For interpretation of the references to colour in this figure legend, the reader is referred to the web version of this article.)

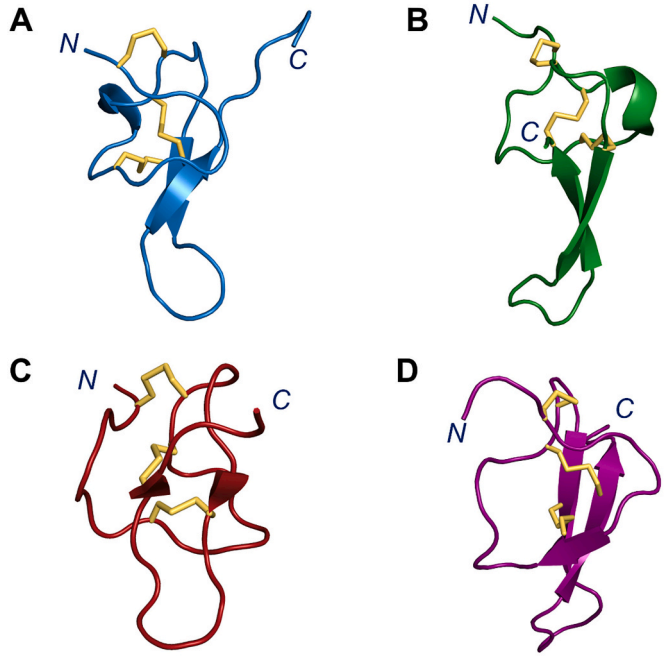

Fig. 8. rTst2 and structure homologues. A. rTst2 (blue). B. ω-atracotoxin-HV1 (ω-ACTX-HV1, PDB 1AXH, green), isolated from the Blue Mountains funnel web spider *Hadronyche versuta*, inhibits insect voltage-gated calcium channels. C. Hainantoxin-III (HNTX-III, PDB 2JTB; brick red), isolated from the Chinese Bird Spider *Ornithoctonus hainana*, is a potent and specific antagonist of neuronal tetrodotoxin-sensitive voltage-gated (Na_V) channels. D. Tachystatin B1 (PDB 2DCV; magenta), an antimicrobial peptide isolated from the Japanese horseshoe crab *Tachypleus tridentatus*. All disulfide bonds are shown as yellow sticks.

paralysis or death observed within 24 h. In comparison, neurotoxic spider-venom peptides with insecticidal properties caused paralysis and death at a much lower dose of 0.005 μg per fly in *D. melanogaster* [59].

4. Discussion

In this study, we characterised a novel peptide, Tst2, by employing both structural (NMR) and functional (electrophysiology and cytotoxicity assays) approaches. Tst2 was identified in a recent proteotranscriptomic analysis of the venom from the Australian sea anemone *Telmatactis stephensoni* [28], a highly venomous species that causes prolonged skin rash and lesions [39,40]. Tst2, the second peptide identified and characterised from *T. stephensoni* after SA8 (a 49-amino acid residue peptide that is a member of the sea anemone 8 family) [28,30], was tentatively designated U-IPTX-Tst2 in accordance with the naming system suggested by Oliveira et al. [41]. As Tst2 showed inhibition of TRPV1, it could now be designated TRPV1-IPTX-Tst2 [41], although we have opted to use the shorter name Tst2 throughout our study, pending further functional characterisation.

Tst2 was produced using recombinant expression in *E. coli* periplasm, which proved to be a cost-effective method for peptide production that enabled disulfide formation [47] and uniform labelling for multidimensional heteronuclear NMR studies [65]. The three-dimensional solution structure of rTst2, determined using NMR spectroscopy, revealed the presence of an ICK motif, which is commonly found in peptides from venomous animals, including cone snails, spiders, plants, and fungi [69,70,78]. The acid-sensing ion channel (ASIC) toxin PhcrTx1 and the K_V type 5 toxin BcsTx3 were the first ICK peptides identified in cnidarians, found in the venom of *Phymanthus crucifer* and *Bunodosoma caissarum*, respectively [79,80]. Both peptide toxins display cysteine patterns characteristic of ICK fold (CXnCXnCCXnCXnC, where X is any amino acid residue and n indicates a variable number of amino acid residues), but their disulfide framework and 3D structures remain to be determined [81,82]. As the ICK motif is also highly stable, resistant to denaturation and proteolysis [83], Tst2 may have potential as a molecular tool or therapeutic lead once its selectivity and toxicity profiles are established.

TRPV1 is a non-selective cation channel that is widely expressed in the peripheral and central nervous systems, activated by a range of stimuli, including heat and chemical irritants [84]. It has a significant role in detecting and transmitting noxious stimuli and regulating pain and inflammation [85]. There is growing interest in its involvement in the pathogenesis of neurodegenerative disorders and cancers, where it regulates cell proliferation, migration, and apoptosis. Blocking TRPV1 has proven to be analgesic in various preclinical pain models, including arthritic [86,87] and cancer pain [88]. Sea anemones have yielded several inhibitors of TRPV1, including APHC1 (τ-SHTX-Hcr2b), APHC2 (τ-SHTX-Hcr2c) and APHC3 (τ-SHTX-Hcr2d) from *Heteractis crispa*. These polypeptides have 56 amino acid residues cross-linked by three disulfide bridges, and have been shown to modulate TRPV1 receptor activity in vitro and provide analgesic effects in vivo [89,90]. APHC1 (200 nM) showed ~32% inhibition of capsaicin-induced currents with half-maximal effective concentration of 54 nM [90], whereas weaker inhibition (25%) was observed with 300 nM of APHC3 [91]. Another TRPV1 inhibitor, HCRG21, from the same sea anemone (*Heteractis crispa*), demonstrated 95% inhibition of capsaicin-induced currents through TRPV1, with a half-maximal inhibitory concentration of 6.9 μM [92]. Recombinant rHCRG21 is the first peptide to fully inhibit TRPV1, even though it has a lower affinity for the channel than other known

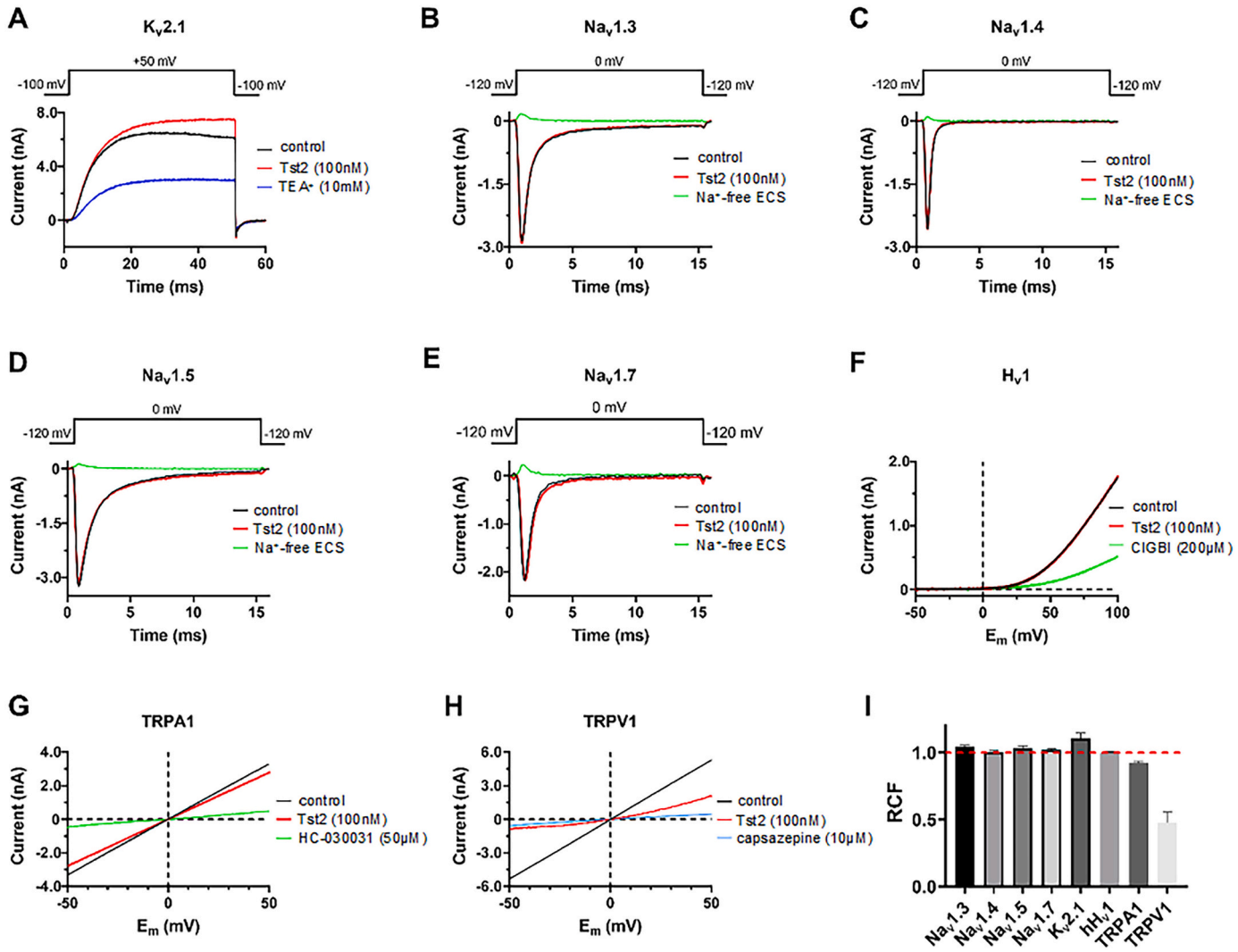

Fig. 9. rTst2 has no inhibitory effect on several voltage-gated ion channels, except TRPV1. Current traces recorded before application of rTst2 (control, black), after 1–2 min perfusion with 100 nM rTst2 (red), and after perfusing the recording chamber with control solutions (Na^+-free ECS solution or specific inhibitors of the ion channel, colored traces). Data are shown for the following channels: $hK_V1.2$ (A), $hNa_V1.3$ (B), $hNa_V1.4$ (C), $hNa_V1.5$ (D), $hNa_V1.7$ (E), hH_V1 (F), hTRPA1 (G), and hTRPV1 (H). For details on the expression systems, solutions, and voltage protocols, see materials and methods. For hH_V1, hTRPA1, and hTRPV1, the currents were recorded in response to a voltage ramp, corrected for ohmic leakage and then displayed as a function of test potential (E_m). The horizonal dashed line shows the zero current level and the vertical dashed line indicates the expected reversal potential for the currents (based on the Nernst equation). (I) Bars represent the mean of 4–6 independent measurements; error bars indicate SEM.

ligands [92]. All of these peptides have Kunitz-type folds and are larger than Tst2.

Macromolecular docking and full atom molecular dynamics simulations performed on the rHCRG21–TRPV1 complex [92] revealed that the positively charged residues (Arg1, Arg18, Lys 28, Arg48, Arg51, and Arg55) interact with acidic amino acid residues lining the TRPV1 pore. In addition, the negatively charged amino acid residues of the peptide could interact with the positively charged extracellular loops of the TRPV1 channel, which further stabilises the rHCRG21-TRPV1 complex. Tst2 contains seven positively charged lysines (Lys2, 10, 12, 23, 28, 29 and 35) and five negatively charged amino acid residues (Asp5, 13, 26 and 34 and Glu17). These charged amino acid residues could play a pivotal role in the interaction between Tst2 and TRPV1, and mutational studies would be informative. rTst2 at 100 nM demonstrated a remarkable inhibition of the TRPV1 current: at equilibrium inhibition, 100 nM rTst2 caused >50% reduction in current amplitude (RCF was 0.48 ± 0.08, $n = 4$). Therefore, Tst2 appears to be a relatively potent inhibitor of TRPV1, making it a promising tool for studying TRPV1 channels and potentially an interesting lead for the development of novel analgesics and anti-inflammatory drugs.

Our structural homology search showed that Tst2 possesses a topology similar to that of antimicrobial ICK-containing peptide tachystatin B1 (PDB: 2DCV), from the Japanese horseshoe crab *Tachypleus tridentatus* [77]. Tachystatin B1 has been shown to possess significant antimicrobial activity against various fungi such as *Candida albicans* and *Pichia pastoris* and gram-positive bacteria (e.g. *Staphylococcus aureus*) [77]. Tachystatin B1 is highly cationic (with a calculated isoelectric point of 12.0) due to the presence of eight Arg residues that form a positively charged patch on its surface and hydrophobic amino acid residues in its core. Such characteristics are widely accepted as important for antimicrobial activity [93]. Tst2, although less cationic than tachystatin B1, is also a cationic peptide, with seven Lys residues and a calculated isoelectric point of 8.39. Furthermore, Tst2 contains several hydrophobic amino acid residues, including Met20, Met32, Ile33, Leu36, and Trp37. The structural homology between Tst2 and tachystatin B1 suggests that Tst2 may exhibit antimicrobial properties, and evaluating its antimicrobial activity would be of interest.

In conclusion, we have shown that Tst2 adopts an ICK motif

structure. The structure was very similar to the structure of several peptide toxins that target ion channels, but, while Tst2 did not show activity against a range of Na_V and K_V channels, or cytotoxic activity against *D. melanogaster* flies, it did show significant inhibition of the TRPV1 channel. The slightly higher expression of Tst2 in epidermis structures (column, pedal disc) is consistent with this peptide having a role in predator deterrence in *T. stephensoni* [4,28]. Furthermore, the activity of Tst2 on the TRPV1 channel suggests that this peptide may play a defensive ecological role by inducing pain, although further work would be needed to confirm this. Mutational studies will also be of interest to identify the key amino acid residues responsible for the promising TRPV1 inhibitory activity.

Accession codes

The NMR chemical shifts have been deposited in BioMagResBank with id 51901 and the solution structure has been deposited in the Protein Data Bank with PDB id code 8SEM.

CRediT authorship contribution statement

Khaled A. Elnahriry: Investigation, Methodology, Data curation, Formal analysis, Visualization, Writing – original draft, Writing – review & editing. **Dorothy C.C. Wai:** Methodology, Data curation, Formal analysis, Visualization, Writing – review & editing, Supervision. **Lauren M. Ashwood:** Investigation, Data curation, Formal analysis, Writing – review & editing. **Muhammad Umair Naseem:** Investigation, Methodology, Data curation, Formal analysis, Visualization, Writing – review & editing. **Tibor G. Szanto:** Investigation, Methodology, Data curation, Formal analysis, Visualization, Writing – review & editing. **Shaodong Guo:** Investigation, Methodology, Data curation, Formal analysis, Visualization, Writing – review & editing. **Gyorgy Panyi:** Data curation, Formal analysis, Writing – review & editing, Supervision. **Peter J. Prentis:** Data curation, Writing – review & editing, Supervision. **Raymond S. Norton:** Conceptualization, Visualization, Writing – review & editing, Supervision.

Declaration of Competing Interest

The authors declare that they have no competing financial interests or personal relationships that could have appeared to influence the results reported in this paper.

Data availability

Data will be made available on request.

Acknowledgements

KE acknowledges support from a Monash University scholarship (FPPS). This work was funded in part by the Hungarian National Research, Development and Innovation Office (K143071 to GP) and by a Stipendium Hungaricum Scholarship from the Tempus Public Foundation (to MUN). We would like to thank Brett Hamilton for his expert advice on mass spectrometry imaging.

Appendix A. Supplementary data

Supplementary data to this article can be found online at https://doi.org/10.1016/j.bbapap.2023.140952.

References

[1] B. Frazão, V. Vasconcelos, A. Antunes, Sea anemone (Cnidaria, Anthozoa, Actiniaria) toxins: an overview, Mar. Drugs 10 (2012) 1812–1851.
[2] Z. Zhang, Animal biodiversity: an introduction to higher-level classification and taxonomic richness, Zootaxa 3148 (2011) 7–12.
[3] D.G. Fautin, Structural diversity, systematics, and evolution of cnidae, Toxicon 54 (2009) 1054–1064.
[4] L.M. Ashwood, R.S. Norton, E.A.B. Undheim, D.A. Hurwood, P.J. Prentis, Characterising functional venom profiles of anthozoans and medusozoans within their ecological context, Mar. Drugs 18 (2020) 202.
[5] P.J. Prentis, A. Pavasovic, R.S. Norton, Sea anemones: quiet achievers in the field of peptide toxins, Toxins 10 (2018) 36.
[6] A. Lotan, L. Fishman, Y. Loya, E. Zlotkin, Delivery of a nematocyst toxin, Nature 375 (1995) 456.
[7] G.M. Watson, D.A. Hessinger, Cnidocyte mechanoreceptors are tuned to the movements of swimming prey by chemoreceptors, Science 243 (1989) 1589–1591.
[8] L. Beress, Biologically active compounds from coelenterates, Pure Appl. Chem. 54 (1982) 1981–1994.
[9] T. Honma, K. Shiomi, Peptide toxins in sea anemones: structural and functional aspects, Mar. Biotechnol. 8 (2006) 1–10.
[10] R.S. Norton, Sea anemone venom peptides, in: A.J. Kastin (Ed.), Handbook of Biologically Active Peptides, San Diego, Elsevier (Academic), 2013, pp. 430–436.
[11] R.S. Norton, Structure and structure-function relationships of sea anemone proteins that interact with the sodium channel, Toxicon 29 (1991) 1051–1084.
[12] O. Castañeda, V. Sotolongo, A.M. Amor, R. Stocklin, A.J. Anderson, A.L. Harvey, A. Engstrom, C. Wernstedt, E. Karlsson, Characterization of a potassium channel toxin from the Caribbean Sea anemone *Stichodactyla helianthus*, Toxicon 33 (1995) 603–613.
[13] K. Kalman, M.W. Pennington, M.D. Lanigan, A. Nguyen, H. Rauer, V. Mahnir, K. Paschetto, W.R. Kem, S. Grissmer, G.A. Gutman, E.P. Christian, M.D. Cahalan, R. S. Norton, K.G. Chandy, ShK-Dap22, a potent Kv1.3-specific immunosuppressive polypeptide, J. Biol. Chem. 273 (1998) 32697–32707.
[14] M.W. Pennington, S.C. Chang, S. Chauhan, R. Huq, R.B. Tajhya, S. Chhabra, R. S. Norton, C. Beeton, Development of highly selective Kv1.3-blocking peptides based on the sea anemone peptide ShK, Mar. Drugs (2015) 529–542.
[15] J.L. Lau, M.K. Dunn, Therapeutic peptides: historical perspectives, current development trends, and future directions, Bioorg. Med. Chem. 26 (2018) 2700–2707.
[16] V. Herzig, B. Cristofori-Armstrong, M.R. Israel, S.A. Nixon, I. Vetter, G.F. King, Animal toxins — Nature's evolutionary-refined toolkit for basic research and drug discovery, Biochem. Pharmacol. 181 (2020), 114096.
[17] M.W. Pennington, A. Czerwinski, R.S. Norton, Peptide therapeutics from venom: current status and potential, Bioorg. Med. Chem. 26 (2018) 2738–2758.
[18] G. Tajti, D.C.C. Wai, G. Panyi, R.S. Norton, The voltage-gated potassium channel $K_V1.3$ as a therapeutic target for venom-derived peptides, Biochem. Pharmacol. 181 (2020), 114146.
[19] E.J. Tarcha, C.M. Olsen, P. Probst, D. Peckham, E.J. Muñoz-Elías, J.G. Kruger, S. P. Iadonato, Safety and pharmacodynamics of dalazatide, a Kv1.3 channel inhibitor, in the treatment of plaque psoriasis: a randomised phase 1b trial, PLoS One 12 (2017), e0180762.
[20] V. Chi, M.W. Pennington, R.S. Norton, E.J. Tarcha, L.M. Londono, B. Sims-Fahey, S. K. Upadhyay, J.T. Lakey, S. Iadonato, H. Wulff, C. Beeton, K.G. Chandy, Development of a sea anemone toxin as an immunomodulator for therapy of autoimmune diseases, Toxicon 59 (2012) 529–546.
[21] M. Muttenthaler, G.F. King, D.J. Adams, P.F. Alewood, Trends in peptide drug discovery, Nat. Rev. Drug Discov. 20 (2021) 309–325.
[22] A. Verdes, P. Anand, J. Gorson, S. Jannetti, P. Kelly, A. Leffler, D. Simpson, G. Ramrattan, M. Holford, From mollusks to medicine: a venomics approach for the discovery and characterisation of therapeutics from Terebridae peptide toxins, Toxins (2016) 117.
[23] M. Holford, M. Daly, G.F. King, R.S. Norton, Venoms to the rescue, Science 361 (2018) 842–844.
[24] G.F. King, Tying pest insects in knots: the deployment of spider-venom-derived knottins as bioinsecticides, Pest Manag. Sci. 75 (2019) 2437–2445.
[25] J.T. Ayala-Sumuano, A. Licea-Navarro, E. Rudino-Pinera, E. Rodriguez, C. Rodriguez-Almazan, Sequencing and de novo transcriptome assembly of *Anthopleura dowii* Verrill (1869), from Mexico, Genom. Data 11 (2017) 92–94.
[26] B. Madio, E.A.B. Undheim, G.F. King, Revisiting venom of the sea anemone *Stichodactyla haddoni*: omics techniques reveal the complete toxin arsenal of a well-studied sea anemone genus, J. Proteome 166 (2017) 83–92.
[27] D. Domínguez-Pérez, A. Campos, A. Alexei Rodríguez, M.V. Turkina, T. Ribeiro, H. Osorio, V. Vasconcelos, A. Antunes, Proteomic analyses of the unexplored sea anemone *Bunodactis verrucosa*, Mar. Drugs 16 (2018) 42.
[28] L.M. Ashwood, E.A.B. Undheim, B. Madio, B.R. Hamilton, M. Daly, D.A. Hurwood, G.F. King, P.J. Prentis, Venoms for all occasions: the functional toxin profiles of different anatomical regions in sea anemones are related to their ecological function, Mol. Ecol. 31 (2022) 866–883.
[29] M.E. Mazzi Esquinca, C.N. Correa, G. Marques de Barros, H. Montenegro, L. Mantovani de Castro, Multiomic approach for bioprospection: investigation of toxins and peptides of Brazilian sea anemone *Bunodosoma caissarum*, Mar. Drugs 21 (2023) 197.
[30] L.M. Ashwood, K.A. Elnahriry, Z.K. Stewart, T. Shafee, M.U. Naseem, Genomic, functional and structural analyses reveal mechanisms of evolutionary innovation within the sea anemone 8 toxin family, BMC Biol. 21 (2023) 121.
[31] M.L. Mitchell, G.Q. Tonkin-Hill, R.A.V. Morales, A.W. Purcell, A.T. Papenfuss, R. S. Norton, Tentacle transcriptomes of the speckled anemone (Actiniaria: Actiniidae: *Oulactis* sp.): venom-related components and their domain structure, Mar. Biotechnol. (NY) 22 (2020) 207–219.
[32] B. Krishnarjuna, C.A. MacRaild, P. Sunanda, R.A.V. Morales, S. Peigneur, J. Macrander, H.H. Yu, M. Daly, S. Raghothama, V. Dhawan, S. Chauhan, J. Tytgat, M.W. Pennington, R.S. Norton, Structure, folding and stability of a minimal

homologue from *Anemonia sulcata* of the sea anemone potassium channel blocker ShK, Peptides 99 (2018) 169–178.
[33] K.A. Elnahriry, D.C.C. Wai, B. Krishnarjuna, N.N. Badawy, B. Chittoor, C. A. MacRaild, B.J. Williams-Noonan, J.M. Surm, D.K. Chalmers, A.H. Zhang, S. Peigneur, M. Mobli, J. Tytgat, P. Prentis, R.S. Norton, Structural and functional characterisation of a novel peptide from the Australian sea anemone *Actinia tenebrosa*, Toxicon 168 (2019) 104–112.
[34] B. Krishnarjuna, J. Villegas-Moreno, M.L. Mitchell, A. Csoti, S. Peigneur, C. Amero, M.W. Pennington, J. Tytgat, G. Panyi, R.S. Norton, Synthesis, folding, structure and activity of a predicted peptide from the sea anemone *Oulactis sp.* with an ShKT fold, Toxicon 150 (2018) 50–59.
[35] P. Sunanda, B. Krishnarjuna, S. Peigneur, M.L. Mitchell, R. Estrada, J. Villegas-Moreno, M.W. Pennington, J. Tytgat, R.S. Norton, Identification, chemical synthesis, structure, and function of a new K_V1 channel blocking peptide from *Oulactis sp*, J. Pept. Sci. 110 (2018).
[36] B. Krishnarjuna, P. Sunanda, J. Villegas-Moreno, A. Csoti, R.A.V. Morales, D.C. C. Wai, G. Panyi, P. Prentis, R.S. Norton, A disulfide-stabilised helical hairpin fold in acrorhagin I: an emerging structural motif in peptide toxins, J. Struct. Biol. 213 (2021), 107692.
[37] M.L. Mitchell, M.A. Hossain, F. Lin, E.L. Pinheiro-Junior, S. Peigneur, D.C.C. Wai, C. Delaine, A.J. Blyth, B.E. Forbes, J. Tytgat, J.D. Wade, R.S. Norton, Identification, synthesis, conformation and activity of an insulin-like peptide from a sea anemone, Biomolecules 11 (2021).
[38] B. Madio, S. Peigneur, Y.K.Y. Chin, B.R. Hamilton, S.T. Henriques, J.J. Smith, B. Cristofori-Armstrong, Z. Dekan, B.A. Boughton, P.F. Alewood, J. Tytgat, G. F. King, E.A.B. Undheim, PHAB toxins: a unique family of predatory sea anemone toxins evolving via intra-gene concerted evolution defines a new peptide fold, Cell. Mol. Life Sci. 75 (2018) 4511–4524.
[39] D.G. Fautin, Hexacorallians of the World, Retrieved from, http://geoportal.kgs.ku.edu/hexacoral/anemone2/index.cfm, 2013.
[40] C.C. Wallace, Hexacorals 1: sea anemones and anemone-like animals (Actiniaria, Zoanthidea, Corallimorpharia, Ceriantharia and Antipatharia), in: The Great Barrier Reef: Biology, environment and management, 2008, pp. 198–207.
[41] J.S. Oliveira, D. Fuentes-Silva, G.F. King, Development of a rational nomenclature for naming peptide and protein toxins from sea anemones, Toxicon 60 (2012) 539–550.
[42] T.U. Consortium, UniProt: the universal protein knowledgebase in 2023, Nucleic Acids Res. 51 (2023) D523–D531.
[43] F. Jungo, A. Bairoch, Tox-Prot, the toxin protein annotation program of the Swiss-Prot protein knowledgebase, Toxicon 45 (2005) 293–301.
[44] J.M. Surm, H.L. Smith, B. Madio, E.A.B. Undheim, G.F. King, B.R. Hamilton, C. A. van der Burg, A. Pavasovic, P.J. Prentis, A process of convergent amplification and tissue-specific expression dominates the evolution of toxin and toxin-like genes in sea anemones, Mol. Ecol. 28 (2019) 2272–2289.
[45] N. Hara, S. Futo, S. Sekiguchi, M. Tsutsui, Y. Tonosaki, A. Fukuchi, A new method to obtain high DNA transformation efficiency of *E. coli* competent cells, Nucleic Acids Res. 16 (1988) 8727.
[46] F.W. Studier, Protein production by auto-induction in high-density shaking cultures, Protein Expr. Purif. 41 (2005) 207–234.
[47] J.K. Klint, S. Senff, N.J. Saez, R. Seshadri, H.Y. Lau, N.S. Bende, E.A. Undheim, L. D. Rash, M. Mobli, G.F. King, Production of recombinant disulfide-rich venom peptides for structural and functional analysis via expression in the periplasm of *E. coli*, PLoS One 8 (2013), e63865.
[48] J. Marley, M. Lu, C. Bracken, A method for efficient isotopic labeling of recombinant proteins, J. Biomol. NMR 20 (2001) 71–75.
[49] M. Mobli, Reducing seed dependent variability of non-uniformly sampled multidimensional NMR data, J. Magn. Reson. 256 (2015) 60–69.
[50] M. Mobli, M.W. Maciejewski, M.R. Gryk, J.C. Hoch, An automated tool for maximum entropy reconstruction of biomolecular NMR spectra, Nat. Methods 4 (2007) 467–468.
[51] F. Delaglio, S. Grzesiek, G.W. Vuister, G. Zhu, J. Pfeifer, A. Bax, NMRPipe: a multidimensional spectral processing system based on UNIX pipes, J. Biomol. NMR 6 (1995) 277–293.
[52] M.W. Maciejewski, A.D. Schuyler, M.R. Gryk, P.R. Moraru II, E.L. Romero, H. R. Ulrich, M. Eghbalnia, F. Livny, J.C. Hoch Delaglio, NMRbox: a resource for biomolecular NMR computation, Biophys. J. 112 (2017) 1529–1534.
[53] W. Lee, M. Tonelli, J.L. Markley, NMRFAM-SPARKY: enhanced software for biomolecular NMR spectroscopy, Bioinformatics 31 (2015) 1325–1327.
[54] N.J. Baxter, M.P. Williamson, Temperature dependence of ^{1}H chemical shifts in proteins, J. Biomol. NMR 9 (1997) 359–369.
[55] L.J. Smith, K.A. Bolin, H. Schwalbe, M.W. MacArthur, J.M. Thornton, C.M. Dobson, Analysis of main chain torsion angles in proteins: prediction of NMR coupling constants for native and random coil conformations, J. Mol. Biol. 255 (1996) 494–506.
[56] P. Güntert, Automated NMR structure calculation with CYANA, Methods Mol. Biol. 278 (2004) 353–378.
[57] C.D. Schwieters, J.J. Kuszewski, N. Tjandra, G. Marius Clore, The Xplor-NIH NMR molecular structure determination package, J. Magn. Reson. 160 (2003) 65–73.
[58] O.P. Hamill, A. Marty, E. Neher, B. Sakmann, F.J. Sigworth, Improved patch-clamp techniques for high-resolution current recording from cells and cell-free membrane patches, Pflugers Arch. 391 (1981) 85–100.
[59] S. Guo, V. Herzig, G.F. King, Dipteran toxicity assays for determining the oral insecticidal activity of venoms and toxins, Toxicon 150 (2018) 297–303.
[60] A.A. Schäffer, L. Aravind, T.L. Madden, S. Shavirin, J.L. Spouge, Y.I. Wolf, E. V. Koonin, S.F. Altschul, Improving the accuracy of PSI-BLAST protein database searches with composition-based statistics and other refinements, Nucleic Acids Res. 29 (2001) 2994–3005.
[61] M. do N Cordeiro, C.R. Diniz, A. do C Valentim, V.R. von Eickstedt, J. Gilroy, M. Richardson, The purification and amino acid sequences of four Tx2 neurotoxins from the venom of the Brazilian 'armed' spider *Phoneutria nigriventer* (Keys), FEBS Lett. 310 (1992) 153–156.
[62] F. Sievers, A. Wilm, D. Dineen, T.J. Gibson, K. Karplus, W. Li, R. Lopez, H. McWilliam, M. Remmert, J. Söding, J.D. Thompson, D.G. Higgins, Fast, scalable generation of high-quality protein multiple sequence alignments using Clustal Omega, Mol. Syst. Biol. 7 (2011) 539.
[63] M. Goujon, H. McWilliam, W. Li, F. Valentin, S. Squizzato, J. Paern, R. Lopez, A new bioinformatics analysis tools framework at EMBL-EBI, Nucleic Acids Res. 38 (2010) W695–W699.
[64] H. McWilliam, W. Li, M. Uludag, S. Squizzato, Y.M. Park, N. Buso, A.P. Cowley, R. Lopez, Analysis tool web services from the EMBL-EBI, Nucleic Acids Res. 41 (2013) W597–W600.
[65] R.S. Norton, Peptide toxin structure and function by NMR, in: G. Webb (Ed.), Modern Magnetic Resonance, Springer, Cham, 2018, pp. 2081–2097.
[66] J.C. Hoch, K. Baskaran, H. Burr, J. Chin, H.R. Eghbalnia, T. Fujiwara, M.R. Gryk, T. Iwata, C. Kojima, G. Kurisu, D. Maziuk, Y. Miyanoiri, J.R. Wedell, C. Wilburn, H. Yao, M. Yokochi, Biological magnetic resonance data bank, Nucleic Acids Res. 51 (2023) D368–D376.
[67] D. Sharma, K. Rajarathnam, ^{13}C NMR chemical shifts can predict disulfide bond formation, J. Biomol. NMR 18 (2000) 165–171.
[68] M. Mobli, G.F. King, NMR methods for determining disulfide-bond connectivities, Toxicon 56 (2010) 849–854.
[69] P.K. Pallaghy, K.J. Nielsen, D.J. Craik, R.S. Norton, A common structural motif incorporating a cystine knot and a triple-stranded beta-sheet in toxic and inhibitory polypeptides, Protein Sci. 3 (1994) 1833–1839.
[70] R.S. Norton, P.K. Pallaghy, The cystine knot structure of ion channel toxins and related polypeptides, Toxicon 36 (1998) 1573–1583.
[71] M. Schubert, D. Labudde, H. Oschkinat, P. Schmieder, A software tool for the prediction of Xaa-Pro peptide bond conformations in proteins based on ^{13}C chemical shift statistics, J. Biomol. NMR 24 (2002) 149–154.
[72] wwPDB consortium, Protein data Bank: the single global archive for 3D macromolecular structure data, Nucleic Acids Res. 47 (2019) D520–D528.
[73] N.A. Baker, D. Sept, S. Joseph, M.J. Holst, J.A. McCammon, Electrostatics of nanosystems: application to microtubules and the ribosome, Proc. Natl. Acad. Sci. U. S. A. 98 (2001) 10037–10041.
[74] L. Holm, P. Rosenström, Dali server: conservation mapping in 3D, Nucleic Acids Res. 38 (2010) W545–W549.
[75] J.I. Fletcher, R. Smith, S.I. O'Donoghue, M. Nilges, M. Connor, M.E.H. Howden, M. J. Christie, G.F. King, The structure of a novel insecticidal neurotoxin, ω-atracotoxin-HV1, from the venom of an Australian funnel web spider, Nat. Struct. Biol. 4 (1997) 559–566.
[76] Z. Liu, T. Cai, Q. Zhu, M. Deng, J. Li, X. Zhou, F. Zhang, D. Li, J. Li, Y. Liu, W. Hu, S. Liang, Structure and function of hainantoxin-III, a selective antagonist of neuronal tetrodotoxin-sensitive voltage-gated sodium channels isolated from the Chinese bird spider *Ornithoctonus hainana*, J. Biol. Chem. 288 (2013) 20392–20403.
[77] N. Fujitani, T. Kouno, T. Nakahara, K. Takaya, T. Osaki, S. Kawabata, M. Mizuguchi, T. Aizawa, M. Demura, S. Nishimura, K. Kawano, The solution structure of horseshoe crab antimicrobial peptide tachystatin B with an inhibitory cystine-knot motif, J. Pept. Sci. 13 (2007) 269–279.
[78] E.A. Undheim, M. Mobli, G.F. King, Toxin structures as evolutionary tools: using conserved 3D folds to study the evolution of rapidly evolving peptides, Bioessays 38 (2016) 539–548.
[79] A.A. Rodríguez, E. Salceda, A.G. Garateix, A.J. Zaharenko, S. Peigneur, O. López, T. Pons, M. Richardson, M. Díaz, Y. Hernández, L. Ständker, J. Tytgat, E. Soto, A novel sea anemone peptide that inhibits acid-sensing ion channels, Peptides 53 (2014) 3–12.
[80] D.J.B. Orts, Y. Moran, C.T. Cologna, S. Peigneur, B. Madio, D. Praher, L. Quinton, E. De Pauw, J.E.P.W. Bicudo, J. Tytgat, J.C. de Freitas, BcsTx3 is a founder of a novel sea anemone toxin family of potassium channel blocker, FEBS J. 280 (2013) 4839–4852.
[81] A.N. Mikov, S.A. Kozlov, Structural features of cysteine-rich polypeptides from sea anemone venoms, Russ. J. Bioorganic Chem. 41 (2015) 455–466.
[82] B. Madio, G.F. King, E.A.B. Undheim, Sea anemone toxins: a structural overview, Mar. Drugs 17 (2019) 325.
[83] N.L. Daly, D.J. Craik, Bioactive cystine knot proteins, Curr. Opin. Chem. Biol. 15 (2011) 362–368.
[84] J.E. Meents, C.I. Ciotu, M.J.M. Fischer, TRPA1: a molecular view, J. Neurophysiol. 121 (2019) 427–443.
[85] S. Christie, G.A. Wittert, H. Li, A.J. Page, Involvement of TRPV1 channels in energy homeostasis, Front. Endocrinol. 9 (2018) 420.
[86] T. Lowin, R.H. Straub, Cannabinoid-based drugs targeting CB1 and TRPV1, the sympathetic nervous system, and arthritis, Arthritis Res. Ther. 17 (2015) 226.
[87] A.M. Obeidat, A. Donner, R.E. Miller, An update on targets for treating osteoarthritis pain: NGF and TRPV1, Curr. Treatm. Opt. Rheumatol. 6 (2020) 129–145.
[88] M. Duitama, Y. Moreno, S.P. Santander, Z. Casas, J.J. Sutachan, Y.P. Torres, S. L. Albarracin, TRP channels as molecular targets to relieve cancer pain, Biomolecules 12 (2021).
[89] S.A. Kozlov, Y.A. Andreev, A.N. Murashev, D.I. Skobtsov, I.A. D'yachenko, E. V. Grishin, New polypeptide components from the *Heteractis crispa* sea anemone with analgesic activity, Russ. J. Bioorg. Chem. 35 (2009) 711–719.

[90] Y.A. Andreev, S.A. Kozlov, S.G. Koshelev, E.A. Ivanova, M.M. Monastyrnaya, E. P. Kozlovskaya, E.V. Grishin, Analgesic compound from sea anemone *Heteractis crispa* is the first polypeptide inhibitor of vanilloid receptor 1 (TRPV1), J. Biol. Chem. 283 (2008) 23914–23921.

[91] Y.A. Andreev, S.A. Kozlov, Y.V. Korolkova, I.A. Dyachenko, D.A. Bondarenko, D. I. Skobtsov, A.N. Murashev, P.D. Kotova, O.A. Rogachevskaja, N.V. Kabanova, S. S. Kolesnikov, E.V. Grishin, Polypeptide modulators of TRPV1 produce analgesia without hyperthermia, Mar. Drugs 11 (2013) 5100–5115.

[92] M. Monastyrnaya, S. Peigneur, E. Zelepuga, O. Sintsova, I. Gladkikh, E. Leychenko, M. Isaeva, J. Tytgat, E. Kozlovskaya, Kunitz-type peptide HCRG21 from the sea anemone *Heteractis crispa* is a full antagonist of the TRPV1 receptor, Mar. Drugs 14 (2016) 229.

[93] R.E. Hancock, T. Falla, M. Brown, Cationic bactericidal peptides, Adv. Microb. Physiol. 37 (1995) 135–175.